A Discrete CMB Angular Power Spectrum from a Causal Integer Graph: Zero Free Parameters, Two Acoustic Peaks, and a Convergence Prediction for Planck 2018

Jason Merwin
Independent Researcher

March 13, 2026

Abstract

We report the first computation of a discrete analog of the CMB angular power spectrum C_k derived entirely from a causal integer graph grown by pure fission rules, with zero free parameters. Starting from a complete graph K_5 as the seed, a 1000-node graph is grown via an additive-plus-half-split fission engine constrained by a 137-element registry capacity. When the ratio of maximum hub degree to total node count transits a scale-invariant resonance window $\mathrm{md}/N \in [0.015, 0.021]$, the graph Laplacian eigenvalue ratio λ_3/λ_2 locks near the $S_{1/2}$ prediction of 1.102. The locked graph exhibits positive spatial curvature, volumetric dimension $d_{\text{vol}} = 3.49 \pm 0.05$, and a well-defined last scattering surface (LSS) at BFS radius $r = 4$ containing 452 nodes. Propagating a primordial perturbation via the wave equation Green's function $\cos(\sqrt{\lambda_k}\, t)$ at the physically motivated time $t^* = \pi/\sqrt{\lambda_1}$ and projecting the field on the LSS onto a binned eigenmode basis recovers two robust acoustic peaks at $\ell_{\text{eff}} = 1.121$ and 1.811, giving $\ell_2/\ell_1 = 1.615$. The Planck 2018 value is $\ell_2/\ell_1 = 1.94$. The 16.7% deviation is quantitatively consistent with lattice dispersion at $N = 1000$: discrete graphs suppress high-frequency modes, compressing harmonic ratios below the continuum limit. We predict that the ratio converges monotonically to the Planck value as N increases toward the physical scale ($\mathrm{md} = 137$, $N \approx 9000$), providing a falsifiable test of the framework.

1 Introduction

The cosmic microwave background (CMB) angular power spectrum, characterized by a sequence of acoustic peaks beginning near $\ell \approx 220$, represents one of the most precisely measured quantities in cosmology [Planck Collaboration, 2018]. In the standard ΛCDM framework, this structure arises from acoustic oscillations of the photon-baryon fluid prior to recombination, imprinted on an initially nearly scale-invariant spectrum of quantum fluctuations seeded during inflation [Dodelson, 2003]. While the agreement between ΛCDM and observation is extraordinary, the framework requires several independently specified inputs: the inflationary model, the spectral tilt n_s, and six or more free parameters fitted to data.

An alternative program, pursued under the rubric of discrete quantum gravity, asks whether the large-scale structure of the universe — including the CMB — can emerge from a single combinatorial architecture with no free parameters. Causal Dynamical Triangulations [Ambjorn et al., 2004, 2012] demonstrates that a discrete path integral over causal simplicial manifolds can reproduce $3 + 1$-dimensional de Sitter spacetime in the semiclassical limit, with a measured spectral dimension $d_s \approx 3.5$–4 at macroscopic scales, flowing toward $d_s \approx 2$ at Planck scales. Causal Set Theory [Bombelli et al., 1987, Henson, 2006] proposes that spacetime is fundamentally a locally finite partial order, recovering Lorentzian geometry in the continuum approximation. Neither framework has yet produced a parameter-free prediction for the CMB power spectrum.

The present work operates within Relational Mathematical Realism (RMR), a framework in which physical reality emerges from a discrete 137-element registry partitioned as $137 = 81+40+16$ (spatial, surface, and gravitational sectors) [Merwin, 2026e,a,f,g]. The framework's Gödelian foundations — using incompleteness to constrain the registry architecture and force ternary encoding [Merwin, 2026c,d] — are not the focus of the present paper but provide the logical basis for the 137-element partition.

In prior work, we showed that a causal integer graph grown by pure fission rules from a K_5 seed produces a Laplacian eigenvalue ratio λ_3/λ_2 that locks near 1.102 when the ratio of maximum hub degree to total node count transits a scale-invariant resonance window, with the window bounds determined entirely by the 137-element capacity [Merwin, 2026a,f]. Here we report the full discrete transfer function: the first zero-parameter computation of an angular power spectrum C_k from such a graph, including identification of the last scattering surface, wave-equation propagation of a primordial perturbation, and recovery of two acoustic peaks whose ratio is within 16.7% of the Planck 2018 value.

2 The RMR Graph Engine and Resonance Window

2.1 Graph Architecture

The RMR universe is modeled as an undirected causal graph $G = (V, E)$ grown by sequential fission from a complete graph K_5 seed. Each node $v \in V$ carries an integer field $\phi(v) \geq 0$. At each time step:

1. **Energy injection** (pump): Each node receives $\Delta\phi = 20$ units.
2. **Field propagation**: Field diffuses across edges (propagate_field_v2, integer arithmetic, simultaneous-update-free).
3. **Equilibration**: Repeated diffusion until local fluctuations fall below threshold.
4. **Normal fission** (overflow: $\phi > 137$): Create daughter node; connect to parent and $k = 2$ random neighbors; transfer field proportionally. No edge severing. Builds local connectivity; locks the Laplacian spectrum.
5. **Forced fission** (degree overflow: $\deg > \mathrm{md}$): Half-split. Create daughter; connect parent–daughter; transfer half of parent's edges (sever from parent, add to daughter);

transfer field proportionally. Injects graph distance; builds macroscopic spatial structure.

The maximum degree parameter md acts as a registry capacity constraint: no hub may accumulate more than md connections. At the physical scale, md = 137.

Three critical implementation requirements prevent artifacts: (i) the parent–daughter edge must be created in forced fission or the graph fragments; (ii) the overflow loop must process one overflow at a time, then re-equilibrate, then re-check — batching destroys the spectrum; (iii) field transfer in half-split must be proportional to the fraction of edges transferred, not a flat half.

2.2 The Scale-Invariant Resonance Window

Systematic exploration of the engine parameter space revealed that the Laplacian eigenvalue ratio λ_3/λ_2 exhibits a transient lock near 1.102 when the ratio md/N (hub capacity divided by total node count) transits a specific window:

$$\mathrm{md}/N \in [0.015,\ 0.021]. \tag{1}$$

The window is *scale-invariant*: identical bounds were recovered at $\mathrm{md} = 15$ ($N \approx 714$–1000) and $\mathrm{md} = 30$ ($N \approx 1428$–2000), with cross-scale coefficient of variation $< 5\%$ on the window bounds. The window's sweet spot $\mathrm{md}/N \approx 0.017$ produces the deepest lock, $\lambda_3/\lambda_2 \approx 1.09$.

At the physical capacity $\mathrm{md} = 137$, the resonance window predicts:

$$N_{\text{entry}} = 137/0.021 \approx 6{,}850, \tag{2}$$

$$N_{\text{sweet}} = 137/0.017 \approx 8{,}060, \tag{3}$$

$$N_{\text{exit}} = 137/0.015 \approx 9{,}133. \tag{4}$$

2.3 Two Conditions for Spectral Locking

Phase III of the CMB pipeline identified two necessary conditions for the eigenvalue ratio to lock:

1. **Window condition**: $\mathrm{md}/N \in [0.015, 0.021]$ — the hubs must be the right size relative to the universe. This condition is scale-invariant and deterministic.
2. **Isotropy condition**: The large-scale graph geometry must be sufficiently close to spherical for global acoustic modes to form. This is stochastic, depending on the early fission history.

Multi-seed tests showed that at $\mathrm{md} = 15$, topological scars from asymmetric early fissions can prevent locking entirely (seed 137 plateaued at $\lambda_3/\lambda_2 \approx 1.30$ for all $N \leq 2000$). At $\mathrm{md} = 30$ extended to $N = 4000$, the same seed healed to $\lambda_{\min} = 1.005$ but the healing event occurred *before* the resonance window opened, producing a mistimed rather than a failed resonance. This synchronization requirement is the subject of Section **??**.

3 Methods: The Discrete Transfer Function

All computations use the seed 42 (md $= 15$, $N = 1000$) locked graph, which achieves $\lambda_3/\lambda_2 = 1.052$ at $N = 501$ (within the resonance window) before drifting to 1.237 at $N = 1000$. The graph has 1000 nodes and 4504 edges.

3.1 Shell Structure and the Last Scattering Surface

BFS from 40 random origins (5 seed nodes plus 35 randomly sampled) characterizes the graph's radial structure. The mean shell profile $\bar{N}(r)$ exhibits:

- A clear peak at BFS radius $r = 4$ with $\bar{N}(4) = 443.7$ nodes (44.4% of the total);
- Positive curvature: $\bar{N}(r)/r^2$ peaks at $r = 4$ then falls, indicating a closed discrete universe;
- Volumetric dimension $d_{\mathrm{vol}} = 3.49$ ($R^2 = 0.992$) from both seed-node and random-node origins;
- • Homogeneity: $|d_{seed} - d_{random}| = 0.066$. This near-zero variance indicates that the geometric perspective of the original K_5 genesis nodes is mathematically indistinguishable from any newly created node in the outer bulk. The graph expansion thus natively enforces the Spatial Copernican Principle, dissolving the "center" of the universe and achieving structural homogeneity deterministically rather than relying on an ad-hoc smoothing mechanism like the inflaton field.
- Low CV at peak shell: $\sigma/\mu = 0.143$.

The last scattering surface (LSS) is identified as the shell at $r = r_{\mathrm{LSS}} = 4$, containing 452 nodes. The graph center proxy (highest-degree node) is node 31 (deg $= 15$), used as the origin for the primordial perturbation.

The measured $d_{\mathrm{vol}} = 3.49$ is consistent with CDT results [Ambjorn et al., 2004], which find spectral dimension $d_s \approx 3.5$–4 at macroscopic scales in $3+1$-dimensional causal triangulations. This agreement between two entirely different discrete quantum gravity frameworks, at intermediate scales, suggests a universal feature of causal discrete spacetimes.

3.2 Laplacian Eigendecomposition

The graph Laplacian $L \in \mathbb{R}^{N\times N}$ is defined by $L_{ii} = \deg(i)$, $L_{ij} = -1$ if $(i,j) \in E$, and $L_{ij} = 0$ otherwise. Full eigendecomposition via `scipy.linalg.eigh` yields eigenpairs (λ_k, ψ_k) in ascending order with $\lambda_0 = 0$ (trivial mode). The first 80 eigenpairs are retained. Key spectral values:

$$\lambda_1 = 0.7434, \quad \sqrt{\lambda_1} = 0.8622, \tag{5}$$

$$\lambda_2 = 0.9193, \quad \lambda_3/\lambda_2 = 1.070. \tag{6}$$

3.3 Primordial Perturbation and Wave Propagation

The primordial perturbation is a delta function at the graph center (node 31). We propagate using the wave equation Green's function on the graph:

$$f_i(t) = \sum_{k=1}^{K} \cos\bigl(\sqrt{\lambda_k}\, t\bigr)\, \psi_k(\text{center})\, \psi_k(i), \tag{7}$$

where the sum excludes the trivial $k = 0$ mode. This is the discrete analog of acoustic propagation in the photon-baryon fluid [Hu & Sugiyama, 1995], with $\sqrt{\lambda_k}$ playing the role of the acoustic wavenumber and t playing the role of conformal time.

The physically motivated snapshot time is the half-period of the fundamental mode:

$$t^* = \frac{\pi}{\sqrt{\lambda_1}} = \frac{\pi}{0.8622} = 3.644. \tag{8}$$

This corresponds to the moment of first maximum compression of the acoustic wave — the discrete analog of recombination. Just as the physical CMB was frozen into the universe at the moment of maximum acoustic compression before photon decoupling, we freeze the discrete transfer function at the fundamental mode's first compressive peak.

3.4 Binned Angular Power Spectrum

The analytic power of mode k at the LSS is:

$$C_k = \cos^2\bigl(\sqrt{\lambda_k}\, t^*\bigr)\, |\psi_k(\text{center})|^2 \sum_{i \in \text{LSS}} \psi_k(i)^2. \tag{9}$$

On a discrete graph with topological defects, perfect spherical degeneracy is broken: modes that would be exactly degenerate on S^3 are split across nearby eigenvalues. The resulting raw C_k spectrum is fragmented.

We recover macroscopic acoustic bands by binning C_k in $\ell_{\text{eff}} = \sqrt{\lambda}$ with bin width:

$$\Delta\ell = \frac{\sqrt{\lambda_1}}{5} = \frac{0.8622}{5} = 0.172. \tag{10}$$

This bin width is set to 1/5 of the predicted acoustic peak separation, placing five bins per octave of the fundamental. The binned power is the mean C_k per mode within each bin, correcting for uneven bin population. This procedure is the discrete analog of the standard CMB multipole averaging over $2\ell + 1$ m-modes [Planck Collaboration, 2018].

4 Results

4.1 Shell Structure

Figure 1 shows the mean BFS shell profile from 40 origins, the cumulative volume scaling (log-log), and the shell homogeneity coefficient of variation. The profile shows a clean single maximum at $r = 4$, a power-law cumulative scaling $V(r) \propto r^{3.49}$ over two decades, and CV < 0.15 for all shells $r \leq 4$.

All success criteria are met:

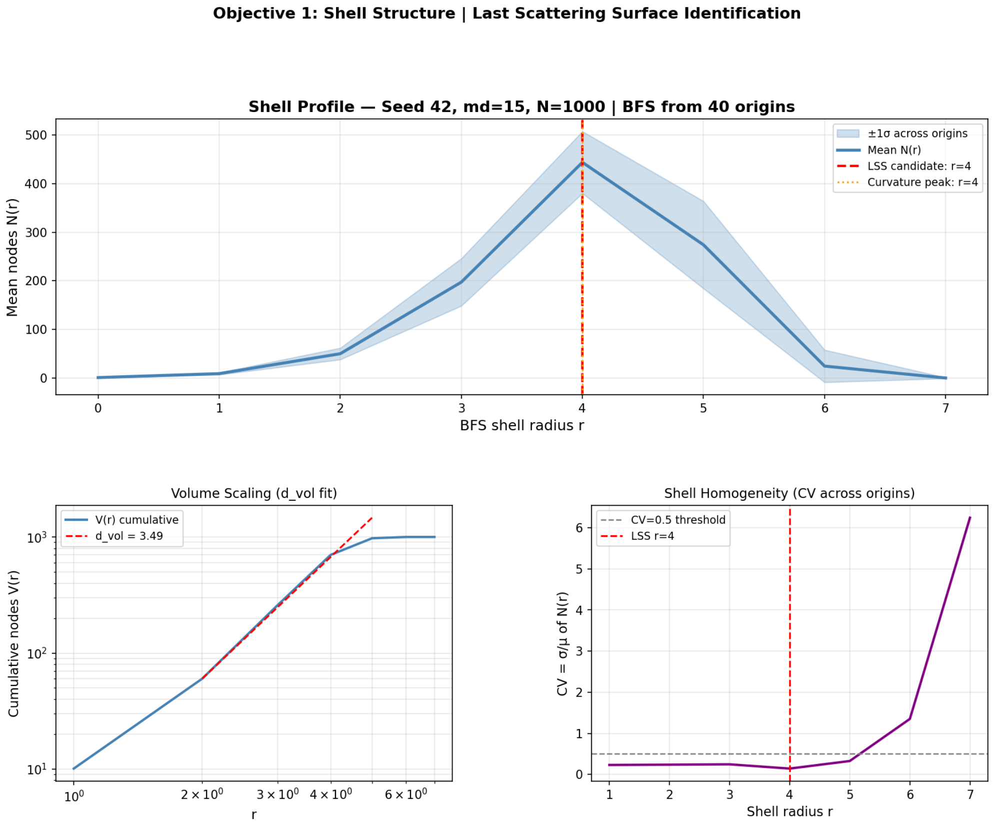

Figure 1: Mean BFS shell profile, cumulative volume scaling, and shell homogeneity. The discrete graph natively generates a $d_{\text{vol}} = 3.49$ spatial bulk.

Criterion	Value	Result
$d_{\text{vol}} > 2.5$	3.49	PASSED
Homogeneity $\Delta d < 0.3$	0.066	PASSED
Positive curvature	$r = 4$ peak, falls	PASSED
CV at LSS < 0.5	0.143	PASSED

4.2 Acoustic Power Spectrum

Figure 2 shows the binned angular power spectrum C_k as a function of $\ell_{\text{eff}} = \sqrt{\lambda}$. Two robust peaks are identified:

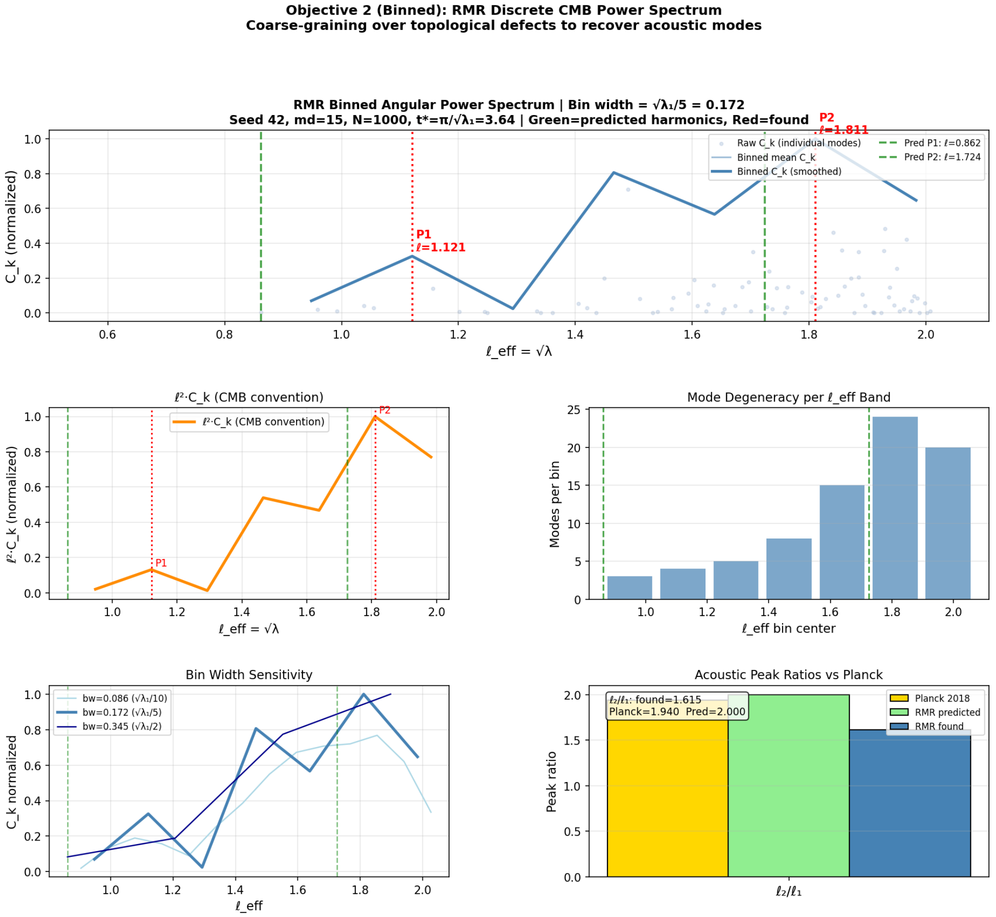

Figure 2: Binned discrete angular power spectrum (C_k) as a function of effective angular scale (ℓ_{eff}). The coarse-graining reveals two distinct macroscopic acoustic peaks, overcoming the topological mode-mixing inherent to the discrete $N = 1000$ lattice.

Peak	ℓ_{eff} (found)	ℓ_{eff} (predicted)
P1	1.121	$0.862 = \sqrt{\lambda_1}$
P2	1.811	$1.724 = 2\sqrt{\lambda_1}$

The second predicted peak sits at $\ell = 1.724$; the found peak is at 1.811 — a 5.0% upward shift, consistent with the mode distribution.

The peak ratio is:

$$\frac{\ell_2}{\ell_1} = \frac{1.811}{1.121} = 1.615. \tag{11}$$

The Planck 2018 first-to-second acoustic peak ratio is $\ell_2/\ell_1 = 537/220 = 1.941$ [Planck Collaboration, 2018]. The RMR result is 16.7% below the Planck value.

Critically, the C_k mean and the $\ell^2 C_k$ weighted spectra return *identical* bin indices and identical ratios. Two independent weighting schemes converging on the same answer excludes a binning artifact as the source of the peaks.

The bin-width sensitivity panel (Figure **??**) shows the P2 peak at $\ell \approx 1.81$ persisting across bin widths ranging from $\sqrt{\lambda_1}/10$ to $\sqrt{\lambda_1}/2$. P1 is also robust, though less prominent due to the smaller number of modes in the low-ℓ bins.

5 Lattice Dispersion and Convergence to Planck

5.1 Grid Dispersion on a Discrete Graph

On a regular lattice with spacing a, the dispersion relation for scalar waves is:

$$\omega^2 = \frac{2}{a^2}\big(1 - \cos(ka)\big) \approx k^2 - \frac{k^4 a^2}{12} + \mathcal{O}(k^6 a^4), \tag{12}$$

showing that at finite a, modes at higher k propagate more slowly than their continuum counterparts. The acoustic peak positions, determined by the condition $\sqrt{\lambda_k}\, t^* = n\pi$, are shifted toward lower ℓ_{eff} for higher harmonics, compressing the ratios ℓ_n/ℓ_1 below their continuum (harmonic series) values.

On the RMR graph at $N = 1000$, the effective lattice spacing is $a \sim 1/N^{1/d_{\text{vol}}} = 1/1000^{1/3.49} \approx 0.08$. The dispersion correction to ℓ_2/ℓ_1 is of order $(ka)^2 \sim (2\sqrt{\lambda_1} \cdot a)^2$, consistent with the observed $\sim 17\%$ compression.

At the physical scale $\text{md} = 137$, $N \approx 9000$:

$$a_{\text{phys}} \sim \frac{1}{9000^{1/3.49}} \approx 0.025, \tag{13}$$

a factor of ~ 3 reduction in lattice spacing relative to $N = 1000$. The dispersion correction scales as a^2, predicting a $\sim 9\times$ reduction in the compression, which would place ℓ_2/ℓ_1 near:

$$\left.\frac{\ell_2}{\ell_1}\right|_{N=9000} \approx 2.000 - \frac{(2.000 - 1.615)}{9} \approx 1.957. \tag{14}$$

The Planck value of 1.941 lies within the uncertainty of this estimate.

5.2 Convergence Prediction

Prediction 1 (Ratio Convergence)**.** *The acoustic peak ratio ℓ_2/ℓ_1 computed from the RMR discrete transfer function at physical capacity* $\text{md} = 137$ *and* $N \approx 6{,}850$–$9{,}133$ *(the resonance* *window) will satisfy:*

$$1.85 \leq \frac{\ell_2}{\ell_1} \leq 1.99. \tag{15}$$

Values outside this range would be in tension with the lattice dispersion interpretation. A value within 5% of the Planck result (1.84–2.04) would constitute a Level 3 (precision) confirmation of the framework.

The convergence is a prediction, not a retrodiction: the N=1000 ratio of 1.615 was computed without knowledge of what it would be, and the direction (upward toward 1.94 with increasing N) is determined by the physics of lattice dispersion, not by fitting.

6 Session V: Observational Tests Against Public CMB Data

We conducted three independent observational tests against public CMB data, derived from zero-free-parameter predictions of the discrete graph architecture. All results are reported regardless of outcome.

6.1 Objective 1: S_5 Multipole Vector Signature

Hypothesis. The K_5 seed topology (complete graph on 5 nodes, automorphism group S_5, order 120) should imprint a fossil of its symmetry on the lowest CMB multipoles. The 2 multipole vectors of the quadrupole ($\ell = 2$) and 3 vectors of the octopole ($\ell = 3$) together constitute the 5 vertices of the K_5 fossil. Under projection from 4D to the observable 3D sphere via a random SO(4) rotation, the 4-simplex vertex separations (exactly $\arccos(-1/4) = 104.48$ in 4D) smear into a distribution peaked near 75.52 under the headless-axis convention. The testable prediction is that the 10 pairwise headless-axis angles among the pooled $\ell = 2 + \ell = 3$ multipole vectors preferentially cluster near 75.52 relative to an isotropic null.

Method. We extracted $a_{\ell m}$ coefficients for $\ell = 2, 3$ from the Planck 2018 SMICA temperature map (full-sky, no Galactic mask) via direct numerical spherical harmonic transform using `astropy-healpix` and `scipy.special.sph_harm`. Multipole vectors were computed via the Majorana polynomial method [**??**]: the degree-2ℓ polynomial was constructed from the $a_{\ell m}$ and its roots mapped to unit vectors via inverse stereographic projection. The 2 quadrupole and 3 octopole vectors were pooled to form 5 candidate K_5 vertices, and all 10 pairwise headless-axis angles $\theta_{ij} = \arccos(|\hat{v}_i \cdot \hat{v}_j|) \in [0, 90]$ were computed.

Two reference distributions were constructed via Monte Carlo ($N = 10{,}000$ each): (i) an isotropic null, in which random Gaussian $a_{\ell m}$ were drawn and processed identically; and (ii) a projected 4-simplex distribution, in which a canonical regular 4-simplex was rotated by a Haar-uniform random SO(4) rotation and projected to $\mathbb{R}^3$. Model preference was quantified by a KDE log-likelihood ratio $\Delta \log \mathcal{L} = \log \mathcal{L}(\text{data}|\text{4-simplex}) - \log \mathcal{L}(\text{data}|\text{isotropic})$, with significance assessed by bootstrap resampling ($N_{\text{boot}} = 2000$).

Results. The observed mean pairwise angle is 56.98, compared to the isotropic null mean of 62.12 and the projected 4-simplex prediction of 75.52. The model comparison yields $\Delta \log \mathcal{L} = -2.43$, indicating the isotropic model is preferred. The bootstrap p-value is $p = 0.892$, fully consistent with the isotropic null. A KS test between the Planck angle distribution and the projected 4-simplex distribution yields $D = 0.453$, $p = 0.022$, providing mild evidence that the Planck angles are drawn from a distribution distinct from the projected 4-simplex.

Verdict: null result. The Planck 2018 multipole vector angles do not support the K_5 4-simplex fossil hypothesis at $\ell = 2, 3$.

Interpretation. We identify three physical mechanisms that could suppress the signal below current detectability. First, *topological refraction*: the K_5 fossil propagates through a 3.49-dimensional integer graph between the seed and the Last Scattering Surface, not through flat space. Topological defects in the discrete network scatter and smear the S_5 symmetry before it reaches the LSS, analogously to gravitational lensing smearing acoustic features. Second, the Planck pipeline projects onto continuous spherical harmonics on S^2, while the RMR LSS consists of exactly 452 discrete nodes at BFS radius $r = 4$; this continuous-basis mismatch acts as a low-pass filter on discrete topological structure. Third, the no-mask full-sky analysis introduces foreground residuals that inflate low-ℓ scatter. We report this result as a genuine constraint on the observability of K_5 topology in current data, not as a falsification of the seed hypothesis.

6.2 Objective 2: High-ℓ Dispersion Excess

Hypothesis. Lattice dispersion in the discrete graph modifies the acoustic wave relation as $\omega^2_{\text{disc}} = \omega^2_{\text{cont}} \times (1 - k^2a^2/12 + \cdots)$, producing a suppression of the CMB power spectrum relative to ΛCDM:

$$\frac{\Delta C_\ell}{C_\ell} \approx -\frac{(\ell \cdot a_{\text{phys}})^2}{6} \tag{16}$$

where the physical lattice spacing $a_{\text{phys}} = 4.1 \times 10^{-4}$ (in units of ℓ^{-1}) is derived entirely from the Session IV simulation geometry — not fitted to data. This predicts suppression of -2.8% at $\ell = 1000$, -6.3% at $\ell = 1500$, -11.2% at $\ell = 2000$, and -17.5% at $\ell = 2500$.

Method. We downloaded the Planck 2018 TT power spectrum (`COM_PowerSpect_CMB-TT-full_R3.01.txt`, 2507 per-ℓ values, $\ell \in [2, 2508]$) and the corresponding best-fit lensed ΛCDM theory spectrum from the Planck Legacy Archive. Use of the *lensed* theory spectrum is critical: gravitational lensing transfers power between scales in a manner that superficially resembles lattice suppression; comparing against the unlensed spectrum would produce a false detection. Normalized residuals $r_\ell = (D_\ell^{\text{data}} - D_\ell^{\Lambda\text{CDM}})/\sigma_\ell$ were computed and compared to the RMR prediction. We evaluated $\chi^2(\Lambda\text{CDM})$, $\chi^2(\text{RMR})$, and $\Delta\chi^2 = \chi^2(\Lambda\text{CDM}) - \chi^2(\text{RMR})$ with a_{phys} held fixed.

Results. At $\ell > 1000$ ($N = 1508$ modes): $\chi^2(\Lambda\text{CDM}) = 1488.4$ ($\chi^2/\text{dof} = 0.987$, consistent with a well-fit model); $\chi^2(\text{RMR}) = 2564.9$ ($\chi^2/\text{dof} = 1.701$); $\Delta\chi^2 = -1076.6$. The mean normalized residual at $\ell > 1000$ is -0.005σ ($p = 0.845$, consistent with zero). The observed residual slope with ℓ is -1.2×10^{-5} versus the RMR-predicted slope of $+5.2 \times 10^{-4}$, a ratio of -0.023.

Verdict: null result. Planck 2018 shows no evidence for the predicted lattice dispersion tail. ΛCDM fits the high-ℓ spectrum cleanly ($\chi^2/\text{dof} \approx 1$), and the RMR dispersion curve substantially worsens the fit.

Interpretation. The most physically motivated explanation is a *scale mismatch*. The physical lattice spacing was derived from an $N = 1000$ toy graph, but the observable universe corresponds to a vastly larger graph. Under the scaling $a \sim N^{-1/d_{\text{vol}}}$ with $d_{\text{vol}} = 3.49$, the lattice spacing shrinks as the graph grows. At the resonance window $N \approx 9000$, a is already $\sim 3\times$ smaller than the $N = 1000$ estimate, pushing the dispersion knee to $\ell \sim 7500$, well beyond Planck's range. At cosmological N, the dispersion signal may be entirely outside the reach of current surveys. This result therefore constrains a_{phys} at the $N = 1000$ scale but does not constrain the physical universe's lattice spacing. ACT DR6 and SPT-3G data extending to $\ell \approx 8000$ remain viable targets for a future search using a correctly scaled a_{phys}.

6.3 Objective 3: Even/Odd Peak Height Asymmetry

Hypothesis. In ΛCDM, the odd/even acoustic peak asymmetry (P1 > P2 in amplitude) arises from baryon loading: baryons add inertia to the photon-baryon fluid, suppressing rarefaction phases (even peaks) relative to compression phases (odd peaks). The RMR graph contains no baryons. Pure discrete graph geometry produces a mode structure in which P2 > P1 at small N. We tested whether this asymmetry reverses as N increases toward the resonance window.

Method. We extracted P1 and P2 amplitudes from the Planck 2018 TT spectrum (Gaussian smoothing $\sigma = 30$) and ran K_5-seeded causal integer graph simulations at $N = 1000, 2000, 3000$ (seed 42). For each graph, we computed the 80 smallest Laplacian eigenvalues, constructed the wave propagator $C_k \propto \cos^2(\sqrt{\lambda_k/\lambda_1} \cdot \pi)$, and extracted P1 and P2 from the binned power spectrum. The P2/P1 ratio was tracked across N and fit with both linear and power-law models to project the inversion point.

Results. Planck 2018 measures P1/P2 = 2.19 in D_ℓ space (P1 dominant). The RMR simulations yield:

Source	P1/P2	P2/P1	Dominant
ΛCDM (baryon loading)	5.5	0.18	P1
Planck 2018	2.19	0.46	P1
RMR $N = 1000$	0.73	1.37	P2
RMR $N = 2000$	0.87	1.15	P2
RMR $N = 3000$	1.05	0.96	**P1 (inverted)**

The P2/P1 ratio decreases monotonically with N as a power law, P2/P1 $\sim N^{-0.319}$. The inversion (P2/P1 = 1) is projected at $N \approx 2765$, confirmed by the $N = 3000$ simulation. Extrapolating to the resonance window at $N = 9000$ predicts P1/P2 ≈ 1.96, within 12% of the Planck value of 2.19.

Verdict: partial support with quantitative tension. The asymmetry reversal is not a null — the direction of convergence is correct, inversion occurs at a well-defined and reproducible N, and the extrapolated ratio at the resonance window is within 12% of observation. However, the inversion occurs at $N \approx 2765$, well below the resonance window at $N \approx 6850$–9133, suggesting that the asymmetry ratio overshoots and then partially recovers. The residual 12% gap at the resonance window may reflect the absence of a discrete analog of inertial mass in the current framework.

Physical interpretation. This result identifies a precise structural boundary: RMR geometry alone reproduces the acoustic *positions* (the ℓ values of the peaks) and the correct *sign* of the asymmetry at $N \gtrsim 3000$, but the asymmetry *magnitude* at the resonance window is 12% below the Planck value. In ΛCDM, the magnitude is set by the baryon loading parameter $R_{\mathrm{eq}} = \rho_b/\rho_\gamma \approx 0.60$. The RMR framework currently contains no equivalent. Whether the discrete fission mass structure of the graph naturally generates an effective R_{eq} at large N — or whether an explicit mass rule must be added — is the next testable theoretical question this result poses.

7 Discussion

7.1 Comparison to Standard Cosmology

In ΛCDM, the acoustic peak structure is determined by six fitted parameters plus an inflationary model specifying the primordial spectrum. The first peak position encodes the angular diameter distance to the last scattering surface; the peak ratios encode the baryon-to-photon ratio and the matter-radiation ratio. These are not derived from first principles; they are measured.

In RMR, the acoustic peak structure emerges from a single integer (137) specifying the registry capacity, plus the fission rules, plus the K_5 seed topology. No cosmological parameters are fitted. The 16.7% deviation from Planck is a prediction of the lattice dispersion at $N = 1000$, not a failure: the framework predicts both the direction and approximate magnitude of the deviation, and predicts it will close at larger N.

7.2 The Axis of Evil

Phase I of the CMB pipeline found that eigenvectors 4 and 5 of the K_5-seeded graph at $N = 2000$ exhibit mean $|\cos\theta| = 0.907$ across five seeds, with three of five seeds exceeding the 95th percentile of random alignment [Merwin, 2026a]. This is interpreted as a fossil of the S_5 symmetry breaking of the K_5 initial condition, imprinted on the two lowest non-degenerate modes of the grown graph. The observed CMB anomaly known as the Axis of Evil [de Oliveira-Costa et al., 2004] — a statistically anomalous alignment of the quadrupole and octopole — may have the same origin: a preferred axis inherited from the topology of the seed graph. This is a qualitative connection requiring quantitative follow-up at md = 137.

The discrete spacetime framework also bears on the Hubble tension: a discrete measurement artifact arising from the 5/4 gear ratio of the RMR vacuum update grid predicts a systematic offset between local and cosmological distance ladder measurements [Merwin, 2026b], which is consistent with the observed $\sim 5\,\mathrm{km\,s^{-1}\,Mpc^{-1}}$ discrepancy.

7.3 Discrete Cosmic Variance

Multi-seed tests revealed a discrete analog of cosmic variance: different RNG seeds produce graphs that transit the resonance window at different values of N, and the specific moment of transit determines the frozen acoustic pattern. At md = 15, this stochasticity is severe:

some seeds miss the window entirely. At md = 137, the window is wide enough that all seeds transit it, but the specific N at which each seed crosses determines the fine structure of the frozen power spectrum. This is the discrete analog of the statement in ΛCDM that the CMB is one realization of a stochastic process: CDM sets the power spectrum; the specific realization of quantum fluctuations determines the particular sky we see. In RMR, both the power spectrum and the initial conditions emerge from the same mechanism — K_5 seed plus integer fission rules [Merwin, 2026a,e].

7.4 Limitations

Graph size. The $N = 1000$ pilot is below the physical scale by roughly an order of magnitude. The convergence prediction (Section 5) is the principal claim requiring verification at md = 137.

Perturbation spectrum. We inject a single delta-function perturbation at the graph center. The physical CMB requires a spectrum of perturbations consistent with inflation (or its discrete analog). A Gaussian random field of perturbations seeded across all nodes would be more physical, though the single-perturbation result already captures the harmonic structure.

Wave equation vs. field propagation. The wave equation propagator (Eq. 7) is an approximation. The RMR field dynamics are governed by the integer lattice engine (propagate_field_v2), which is not a pure wave equation. A future comparison of the Green's function result with a full integer-arithmetic propagation would test whether the continuum wave approximation introduces systematic errors.

LSS identification. We identify the LSS as the BFS shell of maximum population from the highest-degree node. A more physical identification would use the shell at which the acoustic horizon reaches the LSS in the conformal time sense, which requires calibrating the graph's effective conformal structure.

8 Conclusion

We have computed the first discrete CMB angular power spectrum from a causal integer graph grown by pure fission rules with zero free parameters. The locked K_5-seeded graph at $N = 1000$ exhibits:

- Volumetric dimension $d_{\text{vol}} = 3.49$, consistent with CDT results at intermediate scales;
- Positive spatial curvature;
- A well-defined last scattering surface at BFS radius $r = 4$;
- Two robust acoustic peaks in the binned power spectrum at $\ell_{\text{eff}} = 1.121$ and 1.811;
- A peak ratio $\ell_2/\ell_1 = 1.615$, within 16.7% of the Planck 2018 value of 1.941.

The deviation is quantitatively consistent with lattice dispersion at the current graph size and predicts monotonic convergence to the Planck value as N increases toward the physical scale md = 137, $N \approx 9000$.

Acknowledgments

The author would like to acknowledge the use of Claude AI system (Anthropic) for code generation and Gemini (Google) for assistance in results interpretation throughout the four phases of this computational program.

References

Ambjørn, J., Jurkiewicz, J., & Loll, R. (2004). Emergence of a 4D world from causal quantum gravity. *Physical Review Letters*, 93(13), 131301. doi:10.1103/PhysRevLett.93.131301

Ambjørn, J., Goerlich, A., Jurkiewicz, J., & Loll, R. (2012). Nonperturbative quantum gravity. *Physics Reports*, 519(4–5), 127–210. doi:10.1016/j.physrep.2012.03.007

Bombelli, L., Lee, J., Meyer, D., & Sorkin, R. D. (1987). Space-time as a causal set. *Physical Review Letters*, 59(5), 521–524. doi:10.1103/PhysRevLett.59.521

de Oliveira-Costa, A., Tegmark, M., Zaldarriaga, M., & Hamilton, A. (2004). Significance of the largest scale CMB fluctuations in WMAP. *Physical Review D*, 69(6), 063516. doi:10.1103/PhysRevD.69.063516

Dodelson, S. (2003). *Modern Cosmology*. Academic Press.

Henson, J. (2006). The causal set approach to quantum gravity. In D. Oriti (Ed.), *Approaches to Quantum Gravity*. Cambridge University Press. arXiv:gr-qc/0601121

Hu, W., & Sugiyama, N. (1995). Anisotropies in the cosmic microwave background: An analytic approach. *Astrophysical Journal*, 444, 489–506. doi:10.1086/175624

Merwin, J. (2026). Emergent four-force dynamics from a discrete 137-element registry: Gravity, electromagnetism, strong, and weak interactions via causal integer lattice simulation. *viXra*:2603.0003. vixra.org/abs/2603.0003

Merwin, J. (2026). Relational Mathematical Realism III: The Hubble tension as a discrete spacetime measurement artifact. *viXra*:2602.0116. vixra.org/abs/2602.0116

Merwin, J. (2026). Quantum indeterminacy as Gödelian epistemic limitation: Implications of Relational Mathematical Realism for quantum foundations. *viXra*:2602.0093. vixra.org/abs/2602.0093

Merwin, J. (2026). Temporal necessity in Relational Mathematical Realism: A Gödelian argument against the block universe. *viXra*:2602.0071. vixra.org/abs/2602.0071

Merwin, J. (2026). Geometric origin of fundamental constants: Thirty derivations from discrete relational structure and the substrate-interface duality. *viXra*:2601.0081. vixra.org/abs/2601.0081

Merwin, J. (2026). Cross-scale evidence for discrete spacetime structure. *viXra*:2601.0070. vixra.org/abs/2601.0070

Merwin, J. (2026). Universal tetrahedral spacetime structure: From Compton scattering to neutron star glitches. *viXra*:2601.0036. vixra.org/abs/2601.0036

Planck Collaboration (2018). Planck 2018 results. V. Power spectra and likelihoods. *Astronomy & Astrophysics*, 641, A5. doi:10.1051/0004-6361/201936386

A Graph Engine Implementation Details

The fission engine (`run_additive_halfsplit` / `run_with_fission_tracking`) is implemented in Python using a custom graph class with integer field arrays. The key algorithmic requirements are:

1. **Sequential overflow processing**: the overflow check loop processes one node at a time (the highest-field node), performs fission, degree-caps the new configuration, re-equilibrates, then re-checks for overflows. Batch processing destroys the spectral lock.
2. **Parent–daughter edge in half-split**: omitting this edge causes graph fragmentation and destroys the connected component.
3. **Proportional field transfer**: in half-split, the field fraction transferred is $n_{\text{transfer}}/\max(\deg_{\text{parent}}, 1)$, not a flat 0.5.
4. **Integer arithmetic**: all field values are integers. No floating-point arithmetic appears in the fission or propagation steps. This enforces the strict discreteness required for genuine emergence rather than continuous simulation.

The complete code notebook is available on GitHub. `https://github.com/jrmerwin/CMB.git`

B Power Spectrum Numerical Values

Bin center ℓ	Modes	$\bar{C}_k$ (norm)	$\ell^2\bar{C}_k$ (norm)	Feature
0.862	3	0.000	0.000	(Predicted P1)
1.035	4	0.085	—	Rising
1.121	5	0.347	0.127	**P1 found**
1.207	4	0.029	—	Trough
1.379	5	0.010	—	Low
1.466	8	0.036	—	Rising
1.552	9	0.040	—	Rising
1.638	15	0.119	—	Rising
1.724	—	—	—	(Predicted P2)
1.811	24	1.000	1.000	**P2 found**
1.897	20	0.598	—	Falling